

---

# Efficient Er/O doped silicon photodiodes at communication wavelengths by deep cooling

Xingyan Zhao<sup>1</sup>, Kaiman Lin<sup>1</sup>, Sai Gao<sup>2</sup>, Huayou Liu<sup>1</sup>, Jiajing He<sup>1</sup>, Xiaoming Wang<sup>1</sup>, Huimin Wen<sup>1</sup>,  
Yaping Dan<sup>1\*</sup>

<sup>1</sup>University of Michigan Shanghai Jiao Tong University Joint Institute, Shanghai Jiao Tong University,  
Shanghai 200240, China

<sup>2</sup>State Key Laboratory of Advanced Optical Communication Systems and Networks Department of  
Electronic Engineering, Shanghai Jiao Tong University, Shanghai 200240, China

Email: [Yaping.dan@sjtu.edu.cn](mailto:Yaping.dan@sjtu.edu.cn);

## Abstract

Wide band infrared photodetectors have found a wide range of applications in sensing, communication and spectral analysis. However, the commonly used infrared photodetectors are based on Ge and III-V semiconductors which are not CMOS compatible and therefore have limited applications. There is a huge demand for silicon based infrared photodetectors due to its low-cost and compatibility with CMOS processes. Nevertheless, the spectral bandwidth of Si photodetectors is limited to wavelengths shorter than 1.1  $\mu\text{m}$ . Several approaches have been developed to extend Si photodetection bandwidth to communication wavelengths. Er/O doped Si is a promising approach which however suffers from low infrared responsivities at room temperature when the samples are treated with the standard rapid thermal annealing (RTA). In this work, we applied a novel deep cooling process to treat Er/O doped silicon waveguide photodiodes. In comparison with RTA process, the deep cooling process reduces the defect concentration in silicon by two orders of magnitude, resulting in a

This is the author manuscript accepted for publication and has undergone full peer review but has not been through the copyediting, typesetting, pagination and proofreading process, which may lead to differences between this version and the [Version of Record](#). Please cite this article as [doi: 10.1002/advs.202100137](https://doi.org/10.1002/advs.202100137).

---

two-orders-of-magnitude reduction in leakage current density and an enhanced photoresponsivity to 100mA/W at 1510 nm. The 3dB bandwidth of the silicon waveguide photodiode reaches 30 kHz. The device performance can be further improved by optimizing the deep cooling condition and Er/O doping concentration.

Keywords: Silicon waveguide photodetector, Erbium doping, Deep cooling, Communication Wavelength, Defect

During the past decades, wide band infrared (IR) photodetectors have undergone considerable developments and have found applications in various fields from defense, space science and medical imaging to telecommunication.<sup>1-7</sup> The commonly used integrated IR photodetectors are based on epitaxially grown Ge or III-V semiconductor materials.<sup>8-12</sup> In comparison, Si-based photodetectors are more cost effective and compatible with complementary metal-oxide-semiconductor (CMOS) processes, and therefore are more competitive in the market.<sup>13-18</sup> However, the spectral responses of silicon photodiodes are limited to wavelengths shorter than 1.1  $\mu\text{m}$ , significantly shorter than communications wavelengths ( $\sim 1.55 \mu\text{m}$ ). Approaches have been explored to extend the spectral range of silicon-based photodetectors beyond communication wavelengths. One involves incorporating chalcogen dopants into Si through picosecond or femtosecond laser irradiation.<sup>19-22</sup> Although the room temperature responsivity of 35 mA/W at 1550 nm was achieved using this process, it is not suitable for the integrated circuit application due to the complicated laser annealing process and the non-crystalline Si surface formed by the process.<sup>20, 23</sup> Recently, pulsed laser treatment using nanosecond laser has been reported to form single-crystalline surface on gold ion doped silicon. The resultant Si:Au photodiodes have the maximum room temperature EQE of  $9.3 \times 10^{-5}$  at communication wavelengths.<sup>24</sup> Nevertheless, Au is an important detrimental elements to silicon-based devices and therefore incompatible with the CMOS process.<sup>25, 26</sup>

---

Although silicon hyper doped with silver was made into photodiodes,<sup>27</sup> doping silicon with erbium (often with oxygen)<sup>28-30</sup> is particularly interesting for photodetection since Er/O doped silicon can be also potentially made into silicon light sources at communication wavelength.<sup>31-35</sup> Traditionally, Er/O doped silicon suffers from Er/O precipitation after standard rapid thermal annealing (RTA), which results in strong non-radiative recombination.<sup>36-38</sup> Consequently, the RTA-treated Er/O silicon cannot emit or detect photons at communication wavelengths efficiently at room temperature.<sup>28, 36</sup> Recently, we employed a deep cooling (DC) process to treat the Er/O implanted silicon.<sup>31</sup> The processed samples exhibit a strong photoluminescence at room temperature, two orders of magnitude higher than the samples treated by standard RTA process. In this work, we explore the possibility to use Er/O doped silicon treated by the DC process for high-performance photodetection at communication wavelengths. The samples were first annealed at the high-temperature samples ( $\sim 950^{\circ}\text{C}$ ) and cooled down at a rate of  $1000^{\circ}\text{C/s}$  by flushing with Helium gas that is cooled in liquid nitrogen (77K). The dramatic cooling process suppresses the precipitation of Er/O composites as the Er/O composites dissolved in silicon at high temperature do not have enough time to precipitate. After the process, the Er/O doped Si is further made into a Si waveguide photodiode for the potential applications as integrated optic sensors<sup>39, 40</sup> and integrated interferometric optical gyroscopes<sup>41, 42</sup>.

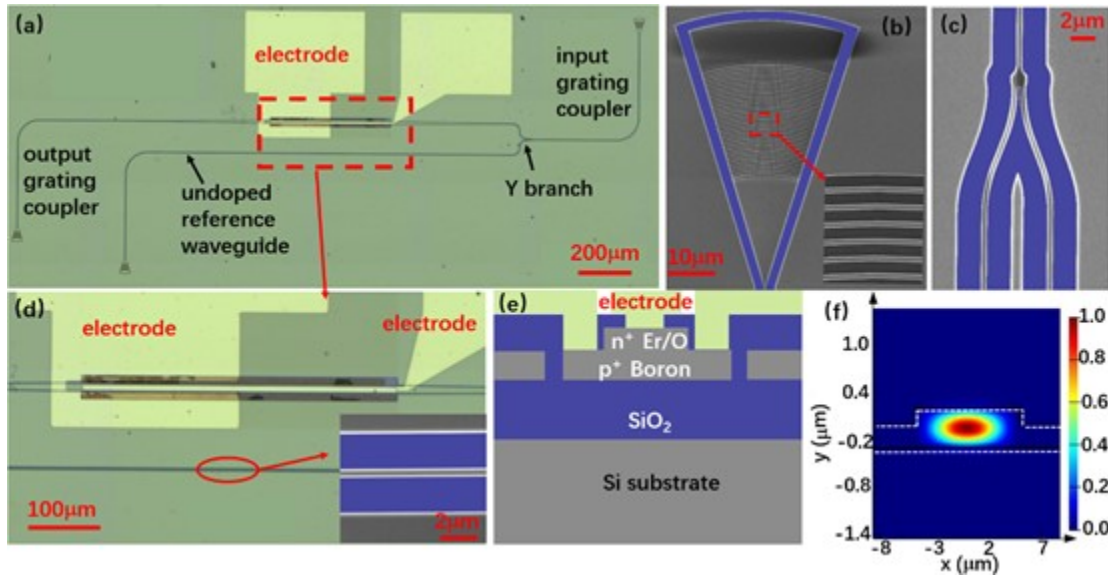


Figure 1 (a) Optical microscope image of the Er/O doped silicon waveguide photodetector. (b) False color SEM image of the grating coupler. (c) False color SEM image of the Y branch. The blue color is  $\text{SiO}_2$  and the grey color represents Si. (d) Optical microscope image of the active region. Inset: SEM image of the silicon waveguide. (e) Cross section of the rib waveguide photodetector. (f) The calculated mode-profile of the rib waveguide.

The Er/O doped Si waveguide photodiodes were fabricated by first patterning the device layer (500nm thick) of an SOI wafer using the standard electron beam lithography and reactive ion etch. An optical microscopic image of the fabricated waveguide photodetector is shown in Figure 1a. Incident light is coupled from a source fiber into the waveguide through a grating coupler ( top right) and splits equally into two parallel waveguides via a Y branch. The output light transmits into free space through the grating coupler at the left bottom and is picked up by a sense fiber. The scanning electron microscopic (SEM) false color images of the fabricated grating couplers and Y branch are shown in Figure 1b and c, respectively. To maximize the coupling efficiency, the grating coupler is designed to have a grating pitch of 728nm, a duty cycle of 0.328 and an etch depth of 100 nm (out of the 500 nm thick device layer). The lower waveguide connecting to the Y branch (see Figure 1a and d) is an

undoped 500nm-wide Si waveguide for reference. The upper waveguide expands to 10  $\mu\text{m}$  wide where the Si rib waveguide is doped with erbium, oxygen and boron ions to form a PN junction diode. The fabrication details are described in the Experimental section. A zoom-in optical microscopic image of the PN junction diode is shown in Figure 1d. The schematic cross-section of the rib waveguide photodetector is depicted in Figure 1e. The top 160 nm of the 500nm thick device layer is doped with Er/O to form the highly doped  $n^+$  region and the bottom layer is implanted with high energy boron ions to form the  $p^+$  region. A deep cooling (DC) process was employed to treat the sample, in which the sample was first inductively heated to 950°C to activate all dopants and then rapidly cooled down to -125°C in 5s by flushing with liquid-nitrogen-cooled Helium gas. The dramatic cooling process suppresses the precipitation of Er/O composites, as a result of which the density of nonradiative recombination centers is significantly reduced. A lower density of nonradiative recombination centers will increase the optical sensitivity of Er-related defects. Optical simulations show that the fundamental mode of the rib waveguide is confined in the rib region (Figure 1f) where the implanted Er/O ions are located. This optical confinement will allow light at communication wavelength to be efficiently absorbed via Er-related defects so that the photoresponsivity is enhanced.

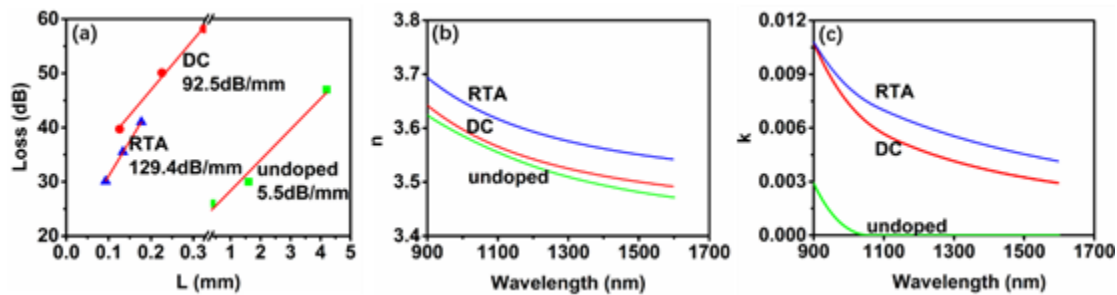


Figure 2 (a) Transmission and absorption loss of the fabricated 500nm-wide Si waveguide at 1550nm. (b) The real part of refractive index of the Er/O doped and undoped Si wafer. (c) The imaginary part of refractive index of the Er/O doped and undoped Si wafer.

---

To quantitatively characterize the absorption efficiency of light at communication wavelength by Er/O doped silicon, we fabricated an array of Si waveguide with the Er/O doping region varying from 90  $\mu\text{m}$  to 320  $\mu\text{m}$  in length. Correspondingly, for both DC and RTA processed sample, the loss increases linearly with the length of the doped region (Fig.2a) at a light wavelength of 1550nm, from which we found a loss of 92.5 dB/mm for DC processed Er/O doped silicon waveguides and 129.4 dB/mm for RTA treated sample. This loss dominantly comes from the absorption of photons via Er/O defects, because the transmission loss in the undoped silicon waveguide is only  $\sim 5.46$  dB/mm (solid squares in Fig.2a).

Analytically, the absorption loss is governed by the following equation eq.(1).<sup>43</sup>

$$\text{loss} = -20\log_{10}(e^{-k2\pi/\lambda}) \quad \text{eq.(1)}$$

where  $k$  is the imaginary part of refractive index and  $\lambda$  is the wavelength. The 92.5 dB/mm and 129.4 dB/mm loss correspond to a  $k$  value of  $\sim 0.0026$  and  $0.0037$  respectively. To verify these values, we prepared two single crystalline silicon wafers that were implanted with Er/O at the same doping concentration and ion implantation energy as the samples in Fig. 2a. One of the samples was treated with the deep cooling process and the other sample was treated with standard RTA process. The refractive index of the Er/O doped silicon wafer and the undoped wafer were measured by ellipsometry. The real part  $n$  and imaginary part  $k$  of the refractive index for the Er/O doped and undoped Si wafer are shown in Fig. 2b and 2c, respectively. Both  $n$  and  $k$  of the Er/O doped wafer are increased in comparison with the undoped silicon wafer while the RTA processed wafer has a higher  $n$  and  $k$  value than the DC treated wafer. The RTA processed sample has a higher  $k$  value likely because the sample has a higher concentration of defects. It is straightforward that a higher concentration of defects leads to a more lossy material, therefore a higher  $k$  value. For the  $n$  value, semiconductor materials with a lower electron concentration will have a larger  $n$  value<sup>44</sup>. Our RTA processed Si wafer has a lower electrical conductivity than DC processed Si wafer. As a result, the  $n$  value is also higher than the DC processed

Si wafer. The imaginary part  $k$  at 1550nm measured by ellipsometry is about 0.003 for DC treated sample and 0.0043 for RTA treated sample. Note that the estimated imaginary value of  $k$  of ellipsometric results from both DC- and RTA-treated samples are slightly higher than the values calculated from loss measurement of the corresponding waveguides. It is probably because the ellipsometric measurements reflect the index of materials near the silicon surface where the Er/O impurities have a maximum concentration. In contrast, the loss measurements accounts for the averaged effect of all Er/O impurities.

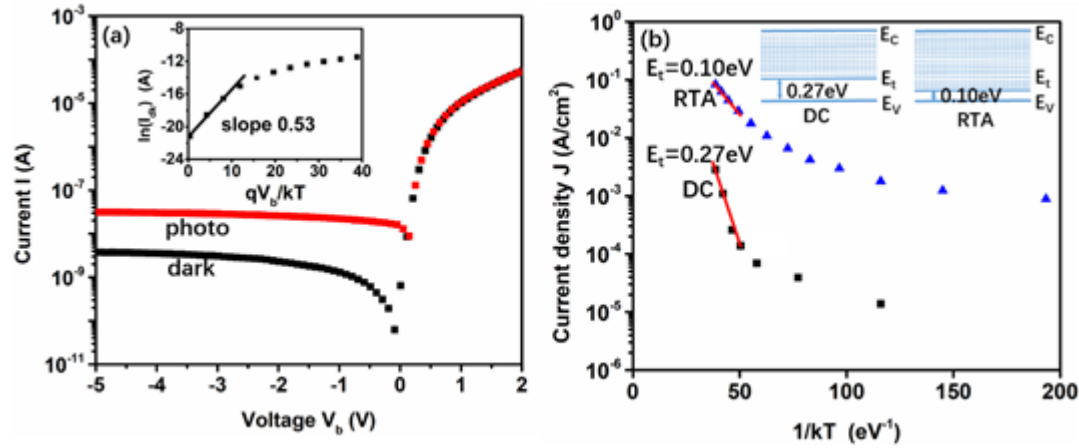


Figure 3 (a) photo and dark  $I$ - $V$  curves of the fabricated Er doped pin photodetector. Inset:  $\ln(I_{dk})$  as a function of  $qV_b/kT$ . (b) Temperature dependent dark current density of the deep cooling and RTA processed samples.

Figure 3a shows the current vs voltage ( $I$ - $V$ ) characteristics of the fabricated Er/O doped waveguide photodetector that was treated with the deep cooling process. The PN junction diode exhibits a reasonably good rectifying behavior with the leakage current four orders of magnitude

smaller than the forward current. The ideality factor of the PN junction diode at small injection is approximately equal to 2 (inset of Fig.3a), indicating that electrons and holes at forward bias dominantly recombine through defects (likely Er-related) in Si bandgap. Under a reverse bias of -2V, a relatively large dark current density ( $\sim 3 \text{ mA/cm}^2$  at room temperature in Fig.3b) is observed via these defects by the thermal generation. Based on the theory of carrier generation-recombination via defects in semiconductors, we derived the dark current density that is dependent on the defect concentration and energy level as shown in eq. (2).

$$J_{dark} = qW_{dep}C_pN_tN_v \exp\left(-\frac{E_g}{KT}\right) \exp\left(\frac{E_c - E_t}{KT}\right) \quad eq. (2)$$

, in which  $q$  is the unit of charge,  $W_{dep}$  the depletion region width,  $C_p$  the hole capture cross-section,  $N_t$  the concentration of defects,  $N_v$  the carrier concentration associated with the valence band,  $E_g$  the bandgap of semiconductor (Si),  $E_c$  the conduction band edge and  $E_t$  the defect energy level. According to eq. (2), the dark current density is highly dependent on temperature. For this reason, we measured the dark current density as a function of temperature for both DC and RTA processed samples as shown in Fig.3b. In comparison with the RTA sample, the dark current density of the DC sample is two orders of magnitude smaller, indicating that the deep cooling process reduces the density of Er-rated defects by two orders of magnitude. This observation is consistent with our recent finding that photoluminescence from the deep-cooling-processed samples is two orders of magnitude stronger than the RTA-processed ones.<sup>31</sup> In Fig.3b, the dark current density for both samples first drops exponentially due to the dominance of the exponential terms in eq. (2). The current later levels off at lower temperature due to the non-exponential term in eq. (2) that is a power function of temperature  $T$ . From the exponential dependence, we found that the defect energy levels are located 0.27 eV and 0.10 eV ( $= E_t - E_v$ ) above the Si valence band for the DC and RTA processed sample, respectively (see Fig.3b). This means that electrons only need to overcome an energy gap of 0.27 eV or 0.10 eV to create the observed dark current. However, the bandgap of Si is 1.12eV. If the defects form a single energy level, there will be still a large energy gap (0.85eV or 1.02 eV) for electrons to thermally excite from the defect energy level  $E_t$  to the conduction band edge. The Arrhenius plot in Fig.3b does not support this assumption of a



single defect energy level. A possible scenario is that the Er/O related defects may have formed a quasi-continuous band from  $E_t$  to the Si conduction band edge, as shown in the inset of Fig.3b. This scenario is consistent with our recent observations that the PL spectrum from the Er/O doped Si has a surprisingly wide broad emission band (0.6eV to 1.1 eV) in addition to the widely reported strong  $\text{Er}^{3+}$  emission peak at 1536nm.<sup>45</sup> Similar quasi-continuous band was also observed in sulfur-doped silicon.<sup>46</sup>

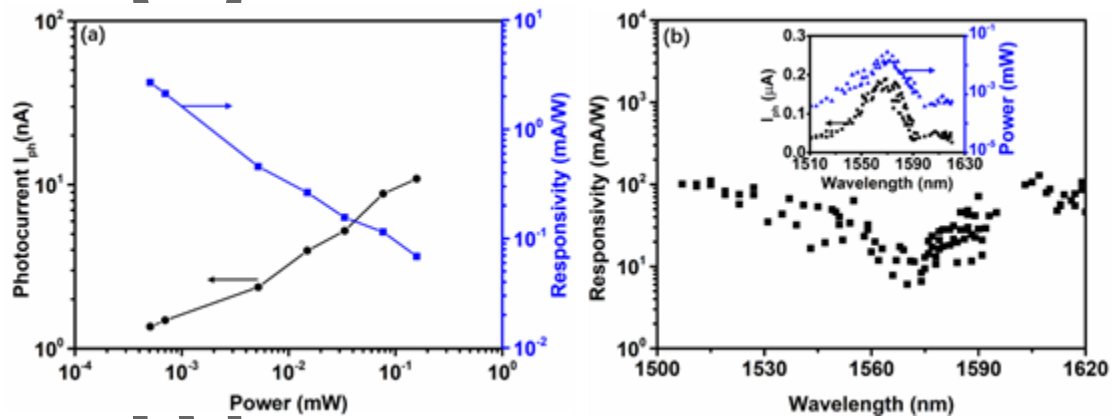


Figure 4 (a) Photocurrent and responsivity at 1570nm as a function of power at bias voltage of -1V. (b) The responsivity spectrum of a 50 $\mu\text{m}$ -long Er photodetector under -5V bias. Inset: The photocurrent and power spectra.

No detectable photocurrent was observed for the sample treated by RTA even when the light at the highest possible intensity is coupled from our tunable laser (Agilent 81640A) into the detector waveguide (upper waveguide in Fig.1a). In contrast, the photodetector treated by the deep cooling process exhibits a relatively large photocurrent at reverse bias (Figure 4a). To find out photoresponsivity of the device, we need to calibrate the light power reaching the Er/O photodetector. Since the incident light splits equally into the reference and detector waveguide via the Y branch, the power reaches the Er/O photodetector can be calculated from the output power at the undoped reference

---

end after taking into account the coupling loss and the Si waveguide transmission loss. Figure 4a shows the power dependent photocurrent and corresponding photoresponsivity of the Er/O doped photodetector that is treated with the deep cooling process. It is surprising to see that the photocurrent increases sublinearly as the light power ramps up, in contrast with the linear increase of photocurrent in standard PIN photo diodes. This may be caused by the relatively low density of Er-related defect states that limit the absorption efficiency of photons when the flux is high. As a result, the photoresponsivity (at 1570nm and bias voltage of -1V) increases (up to 3 mA/W) as the light power reduces. Fig.4b shows the spectral responsivity of a 50 $\mu$ m-long Er photodetector. The spectrum is not uniform mainly due to the non-uniform of the power (inset in Fig.4b) that affects the photoresponsivity (Fig.4a). The maximum photoresponsivity reaches 100mA/W at 1510 nm and bias voltage of -5V, which outperforms the previously reported Er:Si by RTA,<sup>28</sup> Si:Au photodiodes,<sup>24</sup> Si:Ag photodiodes<sup>27</sup> and Si:Zn photodiodes<sup>17</sup> in literatures. Our recent studies show that the activation rate of Er ions is closely related with Er/O doping concentration and deep cooling condition (annealing temperature, annealing time and cooling time). By carefully optimizing these parameters, the responsivity of the Er/O doped Si photodiode can be further improved. Additional experiments show that the spectral response can extend up to  $\lambda = 3.5 \mu\text{m}$  (data not shown here). This is in line with the hypothetical quasi-continuous defect band in the bandgap of silicon and the broad PL emission from the Er/O doped Si that were mentioned above.

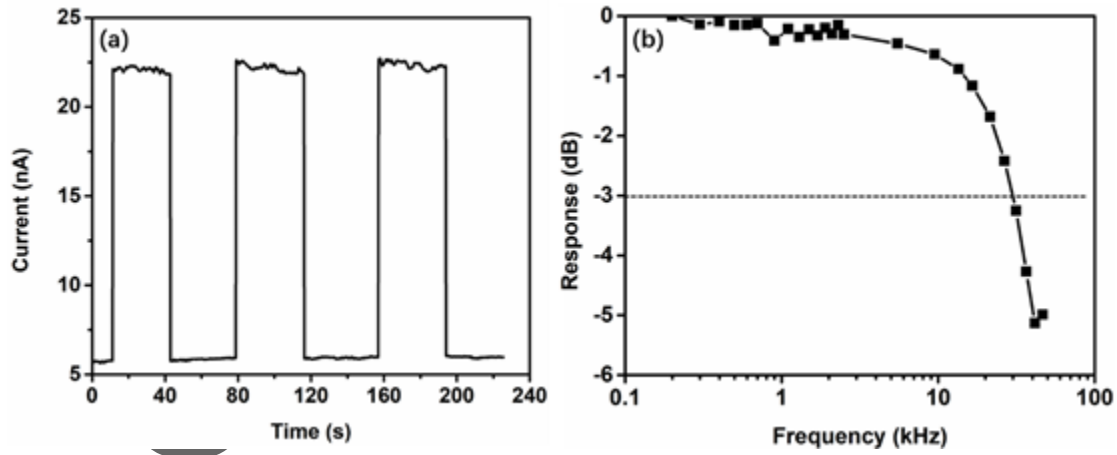


Figure 5 (a) Transient current response of the Er doped photodetector at bias voltage of -1V. (b) Frequency response of the Er doped photodetector at bias voltage -1V.

Transient current measurement (diagram in SI) shows fast and high photoresponses when the light is turn on and turn off periodically, as shown in Figure 5a. The 1550nm light signal is modulated by an acousto-optic (AO) modulator (CETC SGT200-02-N-1D) with a modulation frequency from 200Hz to 100kHz. The modulated light signal is coupled to the SOI waveguide through the grating coupler. The Er/O doped Si PN photodetector is reversely biased and the photocurrent is picked up by a lock-in amplifier SR830. The measured 3dB bandwidth of our 100 $\mu$ m long Er/O photodetector is ~30 kHz (Figure 5b). According to calculation, the junction capacitance of the 100 $\mu$ m long Er/O photodetector is about 6.18pF (see SI for details). From the forward  $I$ - $V$  curve of our Er/O doped Si photodiode, the series resistance  $R_s$  is around  $4 \times 10^4 \Omega$ . With a junction capacitance of 6.18pF, the capacitance charging time is  $\tau_c = R_s C = 2.4 \times 10^{-7} \text{s}$ . If the frequency is dominated by the capacitance, the 3dB bandwidth will be  $f_c = \frac{1}{2\pi\tau_c} = 660 \text{kHz}$ , which is much higher than the 30kHz bandwidth of our Er/O doped Si waveguide photodiode. Therefore, it is concluded that the frequency response of the DC processed Er/O doped Si waveguide photodiode is dominated by the slow back-transfer rate. The back-transfer rate of RTA processed Er/O doped Si wafer is reported to be  $\sim 1.7 \times 10^6 \text{s}^{-1}$  (corresponding

---

to back-transfer time  $5.9 \times 10^{-7}$  s).<sup>29</sup> The DC processed Er/O doped Si wafer will have a much longer back-transfer time since its photoluminescence efficiency is largely enhanced.<sup>31</sup> The DC processed Er/O doped Si waveguide photodiode may have a back transfer time possibly up to  $5 \times 10^{-6}$  s, which leads to a cutoff frequency  $f_{bt} = \frac{1}{2\pi\tau_{bt}} = \frac{1}{2 \times 3.14 \times 5 \times 10^{-6}} = 30$  kHz. The bandwidth of the Er/O photodiode is limited by the slow back-transfer and trap dissociation at a rate of around  $2 \times 10^6$  s<sup>-1</sup>.<sup>29</sup> Although 30 kHz bandwidth is not enough for fiber communication system, the Er/O photodetectors may find applications as integrated optic sensors.<sup>39</sup> Waveguide-based optical sensors are used in a variety of applications such as label-free detection of chemical<sup>40</sup> or integrated interferometric optical gyroscopes for navigation<sup>41, 42</sup>, in which frequency often is not a critical parameter.

## Conclusion

In this work, we applied a DC thermal treatment on Er doped SOI wafer as an alternative to the traditional RTA treatment. The DC treated Er doped Si waveguide showed a reduced absorption loss, as further confirmed by the ellipsometric measurements of  $n$  and  $k$ , due to the reduced defect concentration by the dramatically cooling process of DC. The Er doped Si wafers were further doped with B to form vertical PN junctions and patterned into rib waveguides. The rib waveguide photodiode showed a decreased dark current density and a significantly enhanced photoresponsivity (up to 100 mA/W at 1510 nm) at communication wavelength. Besides, a 3 dB bandwidth around 30 kHz is achieved on the Er/O doped Si rib waveguide photodetector. With the advantages of high responsivity, low-cost and CMOS-compatible process, it is promising for the monolithic integrated IR photodetector application.

## Experimental section

**Device fabrication:** The microfabrication process starts with an SOI wafer with a 500 nm thick device layer and 2  $\mu$ m BOX layer. Photolithography is performed to allow selective doping in the active

---

region. Boron is ion implanted with energy of 110keV and dosage of  $7 \times 10^{14} \text{ cm}^{-2}$ . Er is ion implanted with energy of 200 keV and dosage of  $4 \times 10^{15} \text{ cm}^{-2}$ . O is incorporated with energy of 32 keV and dosage of  $1 \times 10^{16} \text{ cm}^{-2}$ . Electron beam lithography (EBL) and reactive ion etch (RIE) are performed to form the waveguide pattern. The Er/O doped rib waveguide is etched 200nm thickness. The above processes are performed again to form the grating coupler. 200nm thick  $\text{SiO}_2$  is sputtered as the isolating layer. After DC, electrodes are patterned and deposited by photolithography and thermal evaporation. To reduce the absorption by metal electrodes, ITO is applied as the contact material for Er/O doped region. The large electrode pads and contact material for Boron doped region are Ti/Au.

Deep cooling: The deep cooling (DC) process was performed in an upgraded dilatometer (DIL 805A, TA Instruments, see SI Figure S1). The Er/O doped Si samples were first heated at 950 °C for 5 minutes by means of copper coil-based electromagnetic heating and then cooled down to room temperature in 5s by a flush of high purity Helium (99.999%) gas cooled in liquid nitrogen (77 K). Compared to traditional RTA process, the deep cooling method has a much larger cooling rate (up to 1000 °C/s).

## Acknowledgement

The work is financially supported by the special-key project of Innovation Program of Shanghai Municipal Education Commission (2019-07-00-02-E00075), China Postdoctoral Science Foundation (2019M661506) and National Science Foundation of China (NSFC) (no. 61874072, 61904102). The devices were fabricated at the center for Advanced Electronic Materials and Devices (AEMD).

## References

1. Tan, C. L.; Mohseni, H., Emerging technologies for high performance infrared detectors. *Nanophotonics* **2018**, 7 (1), 169-197.

- 
2. Rogalski, A., History of infrared detectors. *Opto-Electronics Review* **2012**, 20 (3).
  3. Rogalski, A., Infrared detectors: an overview. *Infrared Physics & Technology* **2002**, 43 (3), 187-210.
  4. Liu, X.; Kuyken, B.; Roelkens, G.; Baets, R.; Osgood, R. M.; Green, W. M. J., Bridging the mid-infrared-to-telecom gap with silicon nanophotonic spectral translation. *Nature Photonics* **2012**, 6 (10), 667-671.
  5. Zheng, W.; Jia, L.; Huang, F., Vacuum-Ultraviolet Photon Detections. *iScience* **2020**, 23 (6), 101145.
  6. Zheng, W.; Lin, R.; Ran, J.; Zhang, Z.; Ji, X.; Huang, F., Vacuum-Ultraviolet Photovoltaic Detector. *ACS Nano* **2018**, 12 (1), 425-431.
  7. Zheng, W.; Huang, F.; Zheng, R.; Wu, H., Low-Dimensional Structure Vacuum-Ultraviolet-Sensitive ( $\lambda < 200$  nm) Photodetector with Fast-Response Speed Based on High-Quality AlN Micro/Nanowire. *Advanced materials* **2015**, 27 (26), 3921-3927.
  8. Liao, S.; Feng, N. N.; Feng, D.; Dong, P.; Shafiiha, R.; Kung, C. C.; Liang, H.; Qian, W.; Liu, Y.; Fong, J.; Cunningham, J. E.; Luo, Y.; Asghari, M., 36 GHz submicron silicon waveguide germanium photodetector. *Opt Express* **2011**, 19 (11), 10967-72.
  9. Wu, J.; Jiang, Q.; Chen, S.; Tang, M.; Mazur, Y. I.; Maidaniuk, Y.; Benamara, M.; Semtsiv, M. P.; Masselink, W. T.; Sablon, K. A.; Salamo, G. J.; Liu, H., Monolithically Integrated InAs/GaAs Quantum Dot Mid-Infrared Photodetectors on Silicon Substrates. *ACS Photonics* **2016**, 3 (5), 749-753.
  10. Mauthe, S.; Baumgartner, Y.; Sousa, M.; Ding, Q.; Rossell, M. D.; Schenk, A.; Czornomaz, L.; Moselund, K. E., High-speed III-V nanowire photodetector monolithically integrated on Si. *Nature communications* **2020**, 11 (1), 4565.
  11. Yin, T.; Cohen, R.; Morse, M. M.; Sarid, G.; Chetrit, Y.; Rubin, D.; Paniccia, M. J., 31 GHz Ge n-i-p waveguide photodetectors on Silicon-on-Insulator substrate. *Opt Express* **2007**, 15 (21), 13965-71.
  12. Vivien, L.; Osmond, J.; Fedeli, J. M.; Marris-Morini, D.; Crozat, P.; Damlencourt, J. F.; Cassan, E.; Lecunff, Y.; Laval, S., 42 GHz p.i.n Germanium photodetector integrated in a silicon-on-insulator waveguide. *Opt Express* **2009**, 17 (8), 6252-7.
  13. Casalino, M.; Coppola, G.; Iodice, M.; Rendina, I.; Sirleto, L., Near-infrared sub-bandgap all-silicon photodetectors: state of the art and perspectives. *Sensors (Basel)* **2010**, 10 (12), 10571-600.
  14. Rickman, A., The commercialization of silicon photonics. *Nature Photonics* **2014**, 8 (8), 579-582.

- 
15. Masini, G.; Colace, L.; Assanto, G., Si based optoelectronics for communications. *Materials Science and Engineering: B* **2002**, *89* (1), 2-9.
  16. Pavesi, L., Will silicon be the photonic material of the third millenium? . *Journal of Physics: Condensed Matter* **2003**, *15* (26), R1169-R1196.
  17. Grote, R. R.; Souhan, B.; Ophir, N.; Driscoll, J. B.; Bergman, K.; Bahkru, H.; Green, W. M. J.; Osgood, R. M., Extrinsic photodiodes for integrated mid-infrared silicon photonics. *Optica* **2014**, *1* (4).
  18. Li, Y.; Zheng, W.; Huang, F., All-silicon photovoltaic detectors with deep ultraviolet selectivity. *Photonix* **2020**, *1* (1), 15.
  19. Hu, S.; Han, P.; Wang, S.; Mao, X.; Li, X.; Gao, L., Improved photoresponse characteristics in Se-doped Si photodiodes fabricated using picosecond pulsed laser mixing. *Semiconductor Science and Technology* **2012**, *27* (10), 102002.
  20. Carey, J. E.; Crouch, C. H.; Shen, M.; Mazur, E., Visible and near-infrared responsivity of femtosecond-laser microstructured silicon photodiodes. *Opt. Lett.* **2005**, *30* (14), 1773-1775.
  21. Kim, T. G.; Warrender, J. M.; Aziz, M. J., Strong sub-band-gap infrared absorption in silicon supersaturated with sulfur. *Applied Physics Letters* **2006**, *88* (24), 241902.
  22. Bob, B. P.; Kohno, A.; Charnvanichborikarn, S.; Warrender, J. M.; Umezu, I.; Tabbal, M.; Williams, J. S.; Aziz, M. J., Fabrication and subband gap optical properties of silicon supersaturated with chalcogens by ion implantation and pulsed laser melting. *Journal of Applied Physics* **2010**, *107* (12), 123506.
  23. Smith, M. J.; Sher, M.-J.; Franta, B.; Lin, Y.-T.; Mazur, E.; Gradečak, S., The origins of pressure-induced phase transformations during the surface texturing of silicon using femtosecond laser irradiation. *Journal of Applied Physics* **2012**, *112* (8).
  24. Mailoa, J. P.; Akey, A. J.; Simmons, C. B.; Hutchinson, D.; Mathews, J.; Sullivan, J. T.; Recht, D.; Winkler, M. T.; Williams, J. S.; Warrender, J. M.; Persans, P. D.; Aziz, M. J.; Buonassisi, T., Room-temperature sub-band gap optoelectronic response of hyperdoped silicon. *Nature communications* **2014**, *5* (1).
  25. Mallik, K.; Falster, R. J.; Wilshaw, P. R., Semi-insulating silicon using deep level impurity doping: problems and potential. *Semiconductor Science and Technology* **2003**, *18* (6), 517-524.
  26. Graff, K., *Metal impurities in silicon-device fabrication*. Springer Science & Business Media: 2013; Vol. 24.

- 
27. Qiu, X.; Wang, Z.; Hou, X.; Yu, X.; Yang, D., Visible-blind short-wavelength infrared photodetector with high responsivity based on hyperdoped silicon. *Photonics Research* **2019**, *7* (3).
28. Kik, P. G.; Polman, A.; Libertino, S.; Coffa, S., Design and Performance of an Erbium-Doped Silicon Waveguide Detector Operating at 1.5  $\mu\text{m}$ . *J. Lightwave Technol.* **2002**, *20* (5), 834.
29. Hamelin, N.; Kik, P. G.; Suyver, J. F.; Kikoin, K.; Polman, A.; Schönecker, A.; Saris, F. W., Energy backtransfer and infrared photoresponse in erbium-doped silicon p–n diodes. *Journal of Applied Physics* **2000**, *88* (9), 5381-5387.
30. Kenyon, A. J.; Bhamber, S. S.; Pitt, C. W., The infra-red photoresponse of erbium-doped silicon nanocrystals. *Materials Science and Engineering: B* **2003**, *105* (1-3), 230-235.
31. Wen, H.; He, J.; Hong, J.; Jin, S.; Xu, Z.; Zhu, H.; Liu, J.; Sha, G.; Yue, F.; Dan, Y., Efficient Er/O-Doped Silicon Light-Emitting Diodes at Communication Wavelength by Deep Cooling. *Advanced Optical Materials* **2020**, *8* (18), 2000720.
32. Kenyon, A. J., Erbium in silicon. *Semiconductor Science and Technology* **2005**, *20* (12), R65-R84.
33. Yin, Y.; Sun, K.; Xu, W. J.; Ran, G. Z.; Qin, G. G.; Wang, S. M.; Wang, C. Q., 1.53  $\mu\text{m}$  photo- and electroluminescence from Er<sup>3+</sup> in erbium silicate. *Journal of Physics: Condensed Matter* **2008**, *21* (1), 012204.
34. Zheng, B.; Michel, J.; Ren, F. Y. G.; Kimerling, L. C.; Jacobson, D. C.; Poate, J. M., Room - temperature sharp line electroluminescence at  $\lambda = 1.54 \mu\text{m}$  from an erbium - doped, silicon light - emitting diode. *Applied Physics Letters* **1994**, *64* (21), 2842-2844.
35. Lourenco, M. A.; Milosevic, M. M.; Gorin, A.; Gwilliam, R. M.; Homewood, K. P., Super-enhancement of 1.54  $\mu\text{m}$  emission from erbium codoped with oxygen in silicon-on-insulator. *Scientific reports* **2016**, *5*, 37501.
36. Priolo, F.; Franzò, G.; Coffa, S.; Carnera, A., Excitation and nonradiative deexcitation processes of  $\text{Er}^{3+}$  in crystalline Si. *Physical Review B* **1998**, *57* (8), 4443-4455.
37. Kuznetsov, V. P.; Rubtsova, R. A.; Shabanov, V. N.; Kasatkin, A. P.; Sedova, S. V.; Maksimov, G. A.; Krasil'nik, Z. F.; Demidov, E. V., Crystal lattice defects and Hall mobility of electrons in Si: Er/Si layers grown by sublimation molecular-beam epitaxy. *Physics of the Solid State* **2005**, *47* (1), 102-105.
38. Scalese, S.; Franzò, G.; Mirabella, S.; Re, M.; Terrasi, A.; Priolo, F.; Rimini, E.; Spinella, C.; Carnera, A., Effect of O:Er concentration ratio on the structural, electrical, and optical properties of Si:Er:O layers grown by molecular beam epitaxy. *Journal of Applied Physics* **2000**, *88* (7), 4091-4096.



- 
39. K. T. V. Grattan, B. T. M., *Optical Fiber Sensor Technology Chemical and Environmental Sensing* Springer: 1998; Vol. 4, p 113-132.
40. Kunz, R. E.; Cottier, K., Optimizing integrated optical chips for label-free (bio-)chemical sensing. *Analytical and Bioanalytical Chemistry* **2006**, 384 (1), 180-190.
41. Wu, B.; Yu, Y.; Xiong, J.; Zhang, X., Silicon Integrated Interferometric Optical Gyroscope. *Scientific reports* **2018**, 8 (1), 8766.
42. Liu, D.; Li, H.; Wang, X.; Liu, H.; Ni, P.; Liu, N.; Feng, L., Interferometric optical gyroscope based on an integrated silica waveguide coil with low loss. *Opt. Express* **2020**, 28 (10), 15718-15730.
43. Chrostowski, L.; Hochberg, M., *Silicon photonics design: from devices to systems*. Cambridge University Press: 2015.
44. Soref, R.; Bennett, B., Electrooptical effects in silicon. *IEEE journal of quantum electronics* **1987**, 23 (1), 123-129.
45. Jin Hong, H. W., Jiajing He, Jingquan Liu, Yaping Dan, Jens W. Tomm, Fangyu Yue, Junhao Chu, Chungang Duan, Stimulated emission at 1.54  $\mu\text{m}$  from Erbium/Oxygen-doped silicon-based light emitting diodes. *arXiv:2012.04387 [physics.optics]* **2020**.
46. Winkler, M. T.; Recht, D.; Sher, M.-J.; Said, A. J.; Mazur, E.; Aziz, M. J., Insulator-to-Metal Transition in Sulfur-Doped Silicon. *Physical Review Letters* **2011**, 106 (17), 178701.

\*\*\*Short Text and Eye-Catching Figure for the Journal 's Table of Contents (ToC):

Er/O doped Si is a promising approach to realize infrared photodetection. However, it suffers from low infrared responsivities at room temperature when treated with the standard RTA. In this work, a novel deep cooling process is applied to treat Er/O doped silicon waveguide photodiodes. Compared with RTA process, the deep cooling process leads to an enhanced photoresponsivity to 100mA/W at 1510nm at room temperature.

